



Deposited via The University of Leeds.

White Rose Research Online URL for this paper:

<https://eprints.whiterose.ac.uk/id/eprint/114252/>

Version: Accepted Version

Article:

van der Putten, MA, MacKenzie, LE, Davies, AL et al. (2017) A multispectral microscope for in vivo oximetry of rat dorsal spinal cord vasculature. *Physiological Measurement*, 38 (2). pp. 205-218. ISSN: 0967-3334

<https://doi.org/10.1088/1361-6579/aa5527>

© 2017 Institute of Physics and Engineering in Medicine. This is an author produced version of a paper published in *Physiological Measurement*. Uploaded in accordance with the publisher's self-archiving policy.

Reuse

Items deposited in White Rose Research Online are protected by copyright, with all rights reserved unless indicated otherwise. They may be downloaded and/or printed for private study, or other acts as permitted by national copyright laws. The publisher or other rights holders may allow further reproduction and re-use of the full text version. This is indicated by the licence information on the White Rose Research Online record for the item.

Takedown

If you consider content in White Rose Research Online to be in breach of UK law, please notify us by emailing eprints@whiterose.ac.uk including the URL of the record and the reason for the withdrawal request.

A multispectral microscope for *in vivo* oximetry of rat dorsal spinal cord vasculature

Marieke A van der Putten¹, Lewis E MacKenzie¹, Andrew L Davies², Javier Fernandez-Ramos¹, [Roshni A Desai](#)², [Kenneth J Smith](#)² and [Andrew R Harvey](#)¹

¹ School of Physics and Astronomy, University of Glasgow, Glasgow, United Kingdom

² Department of Neuroinflammation, University College London Institute of Neurology, London, United Kingdom

Email: Andy.Harvey@Glasgow.ac.uk

Abstract

Quantification of blood oxygen saturation (SO₂) *in vivo* is essential for understanding the pathogenesis of diseases in which hypoxia is thought to play a role, including inflammatory disorders such as multiple sclerosis (MS) and rheumatoid arthritis (RA). We describe a low-cost multispectral microscope and oximetry technique for calibration-free absolute oximetry of surgically exposed blood vessels *in vivo*. We imaged the vasculature of the dorsal spinal cord in healthy rats, and varied inspired oxygen (FiO₂) in order to evaluate the sensitivity of the imaging system to changes in SO₂. The venous SO₂ was calculated as 67.8 ± 10.4% (average ± standard deviation), increasing to 83.1 ± 11.6% under hyperoxic conditions (100% FiO₂) and returning to 67.4 ± 10.9% for a second normoxic period; the venous SO₂ was 50.9 ± 15.5% and 29.2 ± 24.6% during subsequent hypoxic states (18% and 15% FiO₂ respectively). We discuss the design and performance of our multispectral imaging system, and the future scope for extending this oximetry technique to quantification of hypoxia in inflamed tissue.

Keywords: multispectral imaging, oximetry, spinal cord vasculature

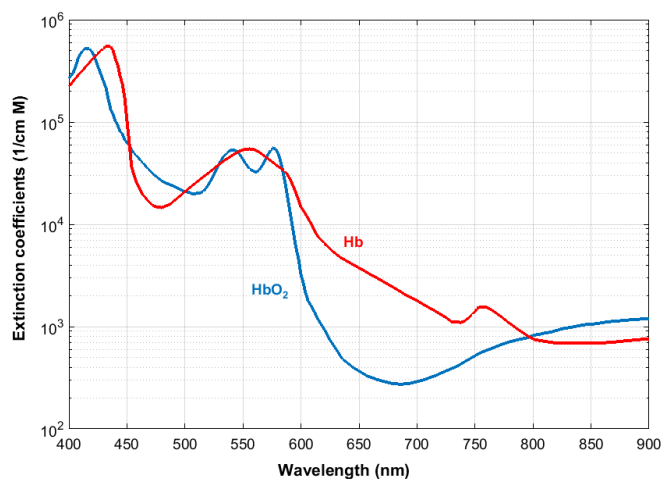
1. Introduction

Tissue hypoxia is associated with inflammation in a range of diseases ([Eltzschig & Carmeliet, 2011](#)), including rheumatoid arthritis (RA) ([Taylor & Sivakumar, 2005](#)), and inflammation of the central nervous system such as occurs in multiple sclerosis (MS) ([Davies, et al., 2013](#)) ([Desai, et al., 2016](#)). Multispectral imaging (MSI) has become established as a method for oximetry with a diverse variety of *in vivo* applications, including non-invasive retinal oximetry ([Mordant, et al., 2011](#); [Choudhary, et al., 2013](#)), ocular microvascular oximetry ([MacKenzie, et al., 2016](#)), and investigation of tumour hypoxia in mouse models ([Sorg, et al., 2005](#)). The principle of MSI oximetry is based upon the oxygen-dependent optical absorption of haemoglobin - the dominant absorber of light in blood. Figure 1 shows the molar extinction coefficients of oxygenated and deoxygenated haemoglobin (values from [Prahl, 1999](#)).

Vascular oximetry using MSI involves estimation of the absorbance of blood vessels at various oxygen-insensitive (isosbestic) and oxygen-sensitive wavelengths. Optical density can be empirically related to SO₂, provided there are known reference values for *in vivo* blood oxygenation (e.g. two-wavelength oximetry in the retina ([Beach, et al., 1999](#))). Unfortunately, for many applications there are no known reference values. Absolute calibration-free oximetry may be achieved however, by determining transmission of a vessel imaged at multiple wavebands, and fitting the measured

49 transmission values to a theoretical optical model. The model we employ here is based upon the
 50 modified Beer-Lambert law, and includes optical absorption, scattering, and other parameters. In this
 51 study we applied a multispectral oximetry algorithm which builds upon previous work by others
 52 (Schweitzer, et al., 1995) (Smith, et al., 2000). In addition, we introduce a contrast-reduction parameter
 53 to account for the effects of variations in thickness of tissue overlying blood vessels and neighbouring
 54 tissue (see Section 2.3).

55



56

57 **Figure 1.** Molar extinction coefficients of oxygenated (HbO₂) and deoxygenated haemoglobin (Hb) as
 58 a function of wavelength (Prahl, 1999).

59 To date, the SO₂ dynamics of the rat spinal cord dorsal veins have not been thoroughly
 60 investigated, with only a few limited studies conducted. Figley et al. (2013) reported use of a
 61 commercial two-wavelength photoacoustic tomography (PAT) imaging system to monitor a temporary
 62 decrease of the dorsal vein SO₂ in rats during hypoxia, however the method for calibration of the PAT
 63 device is not reported. Lesage et al. (2009) and Sharma et al. (2011) studied the use of optical imaging
 64 and non-imaging light-reflectance spectroscopy respectively, to monitor changes in concentration of
 65 oxyhaemoglobin in the rat spinal cord in response to electrical stimulation. Absolute SO₂ values were
 66 not reported, however.

67 Here we introduce a multispectral imaging system suitable for *in vivo* oximetry, and a
 68 complementary multispectral oximetry algorithm. The imaging system was designed and assembled
 69 using low cost, off-the-shelf optical components. We present results of measurement of venous SO₂ in
 70 the dorsal spinal cord vasculature of anaesthetised healthy control rats during normoxia (21% fraction
 71 of inspired oxygen [FiO₂]), hyperoxia (100% FiO₂), and hypoxia (18% and 15% FiO₂). This approach
 72 could be applied to the *in vivo* study of a variety of experimental models in which hypoxia is thought
 73 to play a role.

74

75 2. Methods

76

77 2.1. Multispectral microscope

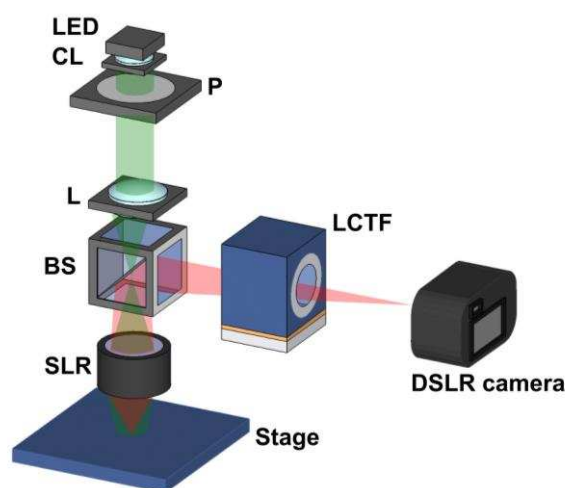
78 A schematic of the multispectral microscope is displayed in Figure 2. The microscope was designed
 79 such that the back focal length of the objective allowed sufficient working space for access to the
 80 exposed spinal cord of a rat under general anaesthesia. The microscope also enabled room for surgical
 81 equipment and was portable so as to be transferred between labs if necessary. A low-magnification,
 82 wide field-of-view system was implemented enabling oximetry of blood vessels across a range of
 83 diameters, and multispectral images between 546 nm and 600 nm were acquired.

84 Illumination was provided by a white LED (*MWWHL3, Thorlabs*) with a collimator lens of focal length
85 40.0 mm (*COP-5A, Thorlabs*). An additional lens (*LA1509, Thorlabs*, $f = 100$ mm) served as a
86 condenser lens for the illumination path. The LED was controlled by a 4-channel driver (*DC4100,*
87 *Thorlabs*). A liquid crystal tuneable filter (*LCTF VIS-7-HC-20, Varispec*) provided electronically-
88 controllable spectral discrimination in 1 nm steps between 400 and 700 nm, with spectral full-width at
89 half maximum of 8 nm. Orthogonal polarisation imaging was used to null specular reflections from
90 blood vessels and ensure that only light which had diffused through tissue was imaged. This was
91 achieved by placing a linear polariser (*LPVISE200-A, Thorlabs*) in the illumination path arranged to
92 be orthogonal to the polarisation axis of the LCTF.

93 A single lens reflex (SLR) served as the microscope objective (*AF Nikkor f/1.8, $f = 50$ mm*),
94 and was configured for finite conjugate imaging. The position of the SLR lens could be manually
95 translated along the z-axis for adjustment of focus. A digital SLR camera (*D300s, Nikon*) was used as
96 the detector.

97 Images were saved as 14-bit RGB NEF (RAW) format and converted to uncompressed
98 greyscale TIFF images for analysis. Greyscale conversion involved selecting either the red or the green
99 channel of the sensor and subtracting the respective dark current channel. The choice of red or green
100 channel was made for each waveband based on which provided higher SNR at that waveband; the red
101 channel was used for $580 \leq \lambda \leq 600$ nm, and the green channel for $546 \leq \lambda \leq 570$ nm. Image acquisition
102 rate was limited by the USB camera interface, which transferred RAW images at a rate of one image
103 every 7.5 seconds; thus a 6-band multispectral dataset was acquired in approximately 45 seconds total.
104 The SLR CMOS detector had 4288 x 2800 pixels and was 23.6 mm by 15.8 mm. The field of view of
105 this configuration was approximately 3.69 mm by 2.47 mm, giving a magnification factor of 6.4
106 corresponding to 0.88 μm per pixel. Automated control of illumination, spectral filtering, and image
107 acquisition was achieved using a custom LabVIEW interface.

108



109

110 **Figure 2.** Schematic of multispectral microscope. LED: light emitting diode; CL: collimating lens; P:
111 linear polariser; L: condenser lens; BS: beamsplitter; LCTF: liquid crystal tuneable filter; SLR lens is
112 oriented with back focal plane towards the target. The illumination path is shown in green, and the
113 imaging path in red.

114

115 2.2. Multispectral image processing and determination of optical transmission

116 Six wavebands were selected for imaging: 546, 560, 570, 584, 590 and 600 nm. Sensitivity to changes
117 in SO_2 was provided by the 560 nm, 590 nm and 600 nm wavebands. The 546 nm, 570 nm and 584 nm

118 wavebands were isobestic, i.e. their absorptions are oxygen-insensitive (see Figure 1). These
 119 wavebands provided close to optimal transmission for oximetry in vessels approximately 100 μm in
 120 diameter. Accurate oximetry is possible for $0.1 < T < 0.7$ (Smith, 1999), where T is the proportional
 121 transmission of light propagated through the blood vessel. Wavelengths longer than 600 nm
 122 are unsuitable, as light of this wavelength is weakly absorbed by oxygenated haemoglobin, resulting in
 123 low contrast and hence sub-optimal transmission for accurate oximetry. Wavelengths below 546 nm
 124 had poor signal-to-noise ratio due to the low intensity of the LED and the low transmission of the LCTF
 125 at these wavelengths, and as such were also deemed unsuitable.

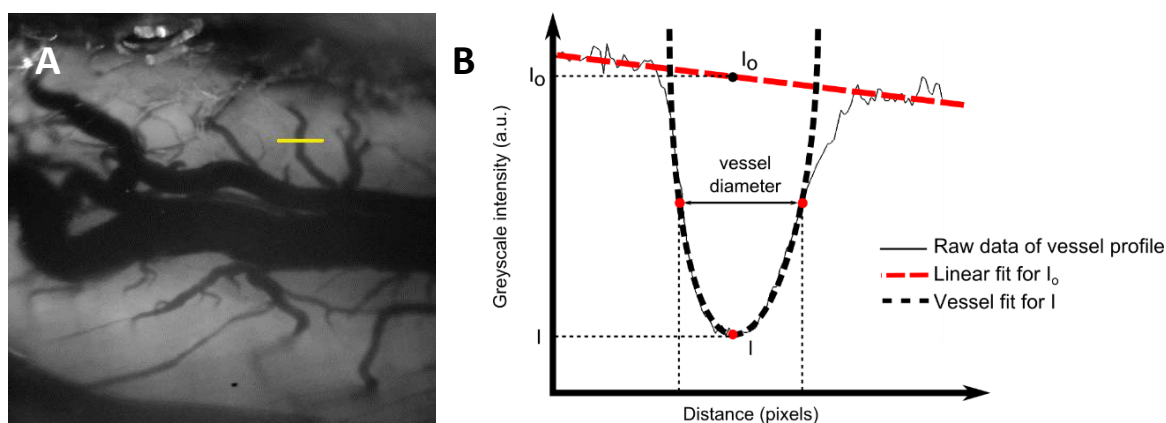
126 All image processing was implemented using custom algorithms in MATLAB. Images at each
 127 waveband were co-registered to form a 6-waveband multispectral data-cube. Vessels were tracked
 128 semi-automatically using user-defined control points. A vessel-profile fitting algorithm (see Figure 3)
 129 was used to estimate vessel diameter at each waveband at each point along the veins. Diameter
 130 estimation was based on the technique described by Fischer et al. (2000); this algorithm determines
 131 edges of the vessel as the points of greatest gradient in the 546 nm line profile. From this, the diameter
 132 of a vessel in pixels, and hence diameter in microns, could be determined. Transmission of vessels at
 133 each wavelength was then determined by a second vessel fitting algorithm. To estimate background
 134 intensity (I_o), a linear fit (the red dashed line in Figure 3B) was applied to points of the line profile
 135 adjacent to the vessel. A second-order polynomial was fitted to the profile inside the vessel to estimate
 136 the intensity at the centre of the vessel (I) (the black dashed line, Figure 3B). The transmission (T) of
 137 the vessel was then calculated by $T = \left(\frac{I}{I_o}\right)$.

138
 139 Only vessels meeting the following inclusion criteria were selected for tracking and oximetry analysis:

- 140 1. Vessels with diameter between 50 and 130 μm .
- 141 2. Vessels producing a transverse line profile at least three times their diameter, and free of any
 142 adjacent vessels, to avoid systemic error in optical transmission calculation.
- 143 3. Vessels without taper - e.g. due to curvature around the spinal cord tissue.

144 Typically only one or two vessels per rat met these inclusion criteria.

145



146
 147 **Figure 3.** (A) Schematic of line profile along a spinal cord vessel – many such line profiles are taken
 148 along each vessel for analysis. (B) Illustration of vessel fitting algorithm used determine vessel diameter
 149 and estimate transmission of light at each waveband.

150

151

152 2.3. Oximetry algorithm

153 A multispectral oximetry algorithm based on the work of [Smith et al. \(2000\)](#) was developed to estimate
 154 SO_2 from transmission values of blood vessels. This algorithm fits a theoretical model of vessel
 155 transmission to experimentally measured transmission values, yielding an estimation of SO_2 . The
 156 theoretical model predicts the wavelength-dependent transmission of a blood vessel of known diameter
 157 by accounting for blood oxygen saturation and incorporating empirical values for extinction and
 158 reduced scattering coefficients reported in the literature ([Prahl, 1999](#); [Bosschaart et al., 2014](#)). Further,
 159 we add an extra parameter – a contrast reduction parameter - to compensate for local variations in tissue
 160 thickness overlying vessels. This tissue tends to add a scattering component which reduces vessel
 161 contrast and hence transmission values, leading to incorrect estimation of SO_2 . This section briefly
 162 describes how the model was derived.

163 From the Beer-Lambert law of optical transmission and absorption, we first defined the optical
 164 density (OD) of a blood vessel as:

$$165 \quad OD = \log_{10}(T) = \varepsilon(\lambda)C_{HbT}d, \quad (1)$$

166 where T ($T = \frac{I}{I_0}$) is the experimentally measured transmission of a vessel as depicted in Fig. 3, d is the
 167 vessel diameter, C_{HbT} is the molar concentration of total haemoglobin, and $\varepsilon(\lambda)$ is the effective optical
 168 extinction coefficient of haemoglobin; $\varepsilon(\lambda)$ is dependent on both the oxygen saturation and
 169 wavelength-dependent molar extinction coefficients $\varepsilon_{HbO_2}(\lambda)$ and $\varepsilon_{Hb}(\lambda)$ of oxygenated and
 170 deoxygenated haemoglobin respectively. We used accepted values from the literature shown in Figure
 171 1 ([Prahl, 1999](#)). These values are derived from human blood, but it has been shown that the difference
 172 between the absorption of light by haemoglobin in rats and humans is minimal ([Zijlstra, et al., 1994](#)).
 173 Defining c_1 and c_2 as proportional concentrations of oxygenated (HbO_2) and deoxygenated (Hb)
 174 haemoglobin respectively, (1) is rewritten as

$$175 \quad OD = (\varepsilon_{HbO_2}(\lambda) c_1 + \varepsilon_{Hb}(\lambda) c_2)d \quad (2)$$

176 where: $c_1 + c_2 = C_{HbT}$, so $c_1 = C_{HbT}SO_2$ and $c_2 = C_{HbT}(1 - SO_2)$, and SO_2 is the oxygen saturation; in other
 177 words, the proportion of oxygenated haemoglobin in the total solution of haemoglobin. It was also
 178 necessary to introduce a parameter to account for the optical scattering properties of blood. (2) is thus
 179 rewritten as:

$$180 \quad OD = C_{HbT}d \left[(\varepsilon_{HbO_2}(\lambda) - \varepsilon_{Hb}(\lambda))SO_2 + \varepsilon_{Hb}(\lambda) \right] + \mu'(\lambda)d \quad (3)$$

181 where the $\mu'(\lambda)$ is the wavelength-dependent reduced scattering coefficient, which considers
 182 wavelength-dependent scattering ([Faber, et al., 2004](#)). By using compiled average values of scattering
 183 coefficients $\mu(\lambda)$ and scattering anisotropy factors $g(\lambda)$, we determined these reduced scattering
 184 coefficients: $\mu'(\lambda) = \mu(\lambda)(1 - g(\lambda))$ ([Bosschaart, et al., 2014](#)).

185 Two parameters, α and β , are also introduced to account for the combination of single-pass
 186 transmission (light diffused through adjacent tissue and back-illuminating the vessel) and double-pass
 187 transmission (light transmitted directly through the vessel and scattered back from distal tissue). This
 188 concept is based on [Smith, et al., \(2000\)](#). Equation (3) is then rewritten in terms of transmission as:

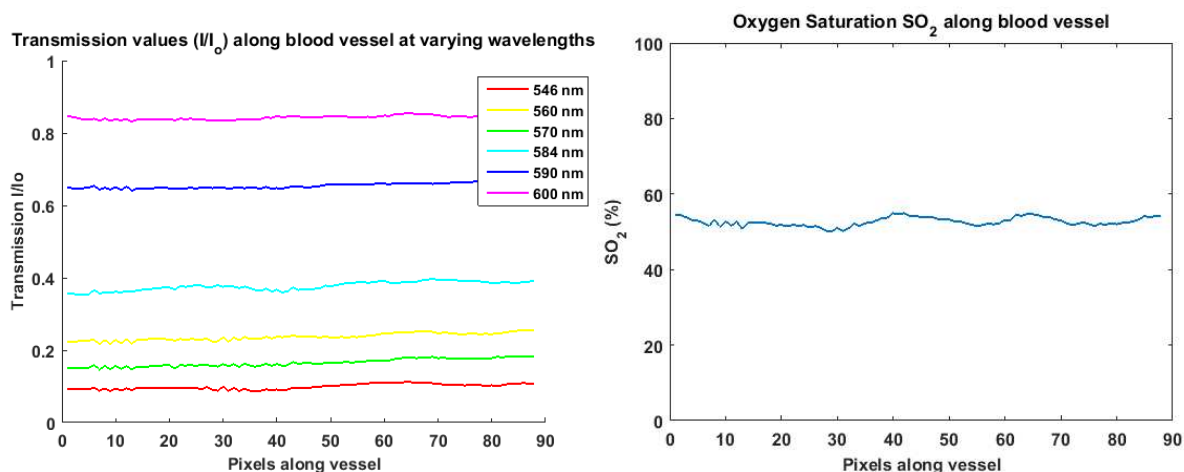
$$189 \quad T(\lambda) = \left(\alpha 10^{-\left(C_{HbT} d \left[(\varepsilon_{HbO_2}(\lambda) - \varepsilon_{Hb}(\lambda))SO_2 + \varepsilon_{Hb}(\lambda) \right] + \mu'(\lambda)d \right)} \right. \\ \left. + \beta 10^{-\left(2C_{HbT} d \left[(\varepsilon_{HbO_2}(\lambda) - \varepsilon_{Hb}(\lambda))SO_2 + \varepsilon_{Hb}(\lambda) \right] + 2\mu'(\lambda)d \right)} \right) \quad (4)$$

202 Finally, it was considered that various factors other than SO₂ may alter the measured
 203 transmission values, such as scattering by overlying tissue. The imaging system itself may also
 204 introduce scattering and hence a loss of contrast. Contrast reduction was incorporated as an increase in
 205 greyscale intensity I_c of both the background and the vessel. Transmission was hence re-defined as
 206 $T'(\lambda) = \left(\frac{I+I_c}{I_o+I_c}\right)$. A contrast parameter K was introduced such that $K = \frac{I_c}{I_o+I_c}$. By substitution, this
 207 yields: $T'(\lambda) = T(\lambda)(1 - K) + K$. Applying this substitution to (4), a final model for transmission was
 208 derived:

$$T'(\lambda) = \left(\alpha 10^{-\left(C_{HbT}(\lambda)d\left[\left(\epsilon_{HbO_2}(\lambda) - \epsilon_{Hb}(\lambda)\right)SO_2 + \epsilon_{Hb}(\lambda)\right] + \mu'(\lambda)d\right)} \right. \\ \left. + \beta 10^{-\left(2C_{HbT}(\lambda)d\left[\left(\epsilon_{HbO_2}(\lambda) - \epsilon_{Hb}(\lambda)\right)SO_2 + \epsilon_{Hb}(\lambda)\right] + 2\mu'(\lambda)d\right)} \right) (1 - K) + K. \quad (5)$$

209 The experimentally measured transmissions are then fitted to (5) using a nonlinear least-squares
 210 fit. Additionally, vessel diameter was allowed to vary from the measured vessel diameter by $\pm 5 \mu m$.
 211 This yields estimated values of α , β , K , and SO₂. The resulting fits were robust, with SO₂
 212 approximately constant along the vessel. Figure 4 presents an illustrative example of experimentally
 213 obtained transmissions along a blood vessel at all six wavebands, and the resulting SO₂ values along
 214 the vessel, as produced by the algorithm.

206



207 **Figure 4.** (A) Example of transmission profile along a tributary vessel. (B) SO₂ estimated by the
 208 multispectral oximetry algorithm along the same vessel.
 209

210

211 2.4. *In vivo* imaging procedure

212 All procedures involving animals were carried out in accordance with the ARRIVE guidelines and the
 213 United Kingdom Home Office Animals (Scientific Procedures) Act 1986. Four female Dark Agouti rats
 214 (average weight 180 g) were used for the control validation study. A laminectomy was performed under
 215 2% isoflurane anaesthesia in room air, and the dorsal aspect of vertebral segment L1 was removed to
 216 expose the cord for imaging. After surgery, the isoflurane was reduced to 1.5% for the remainder of the
 217 experiment, including all imaging. Motion due to animal heart-beat and breathing can provide a
 218 challenge for *in vivo* imaging, but surgical sutures were used to reduce loading of weight on the rat
 219 ribcage and the spinous process rostral to the exposed cord was clamped in place using a modified
 220 hemostatic clamp, minimising motion sufficiently for imaging. Similar strategies have been employed

221 in other studies which imaged the murine spinal cord ([Johannssen & Helmchen, 2010](#)), ([Vinegoni, et](#)
222 [al., 2014](#)), ([Cadotte, et al., 2012](#)).

223 Arterial SO_2 was monitored and recorded throughout the experiment using a pulse-oximeter
224 collar (MouseOx, STARR Life). A homeothermic heating mat and rectal temperature probe maintained
225 the rectal temperature at $37^\circ C$. For each rat, image exposure time for each waveband was optimised to
226 ensure sufficient exposure and to avoid image saturation.

227 Assessing changes in SO_2 due to changes in FiO_2 is an effective way of testing the sensitivity of the
228 oximetry technique. To assess response to changes in FiO_2 in healthy rats, FiO_2 was varied sequentially,
229 with three full multispectral datasets acquired at each stage of the experiment. The following sequence
230 was used: baseline normoxia (21% FiO_2 for 10 minutes), hyperoxia (100% FiO_2 for 10 minutes), return
231 to normoxia (normoxia 2, 21% FiO_2 for 5 minutes), then incrementally decreasing FiO_2 to induce
232 progressive hypoxia (hypoxia 1, 18% and hypoxia 2, 15%; 5 minutes each). Similar protocols have been
233 used in previous oximetry studies ([MacKenzie, et al., 2016](#)), and have been shown to produce a
234 sequence of SO_2 changes that is clearly distinct from normal physiological variation.

235

236 3. Results

237

238 3.1. Images acquired

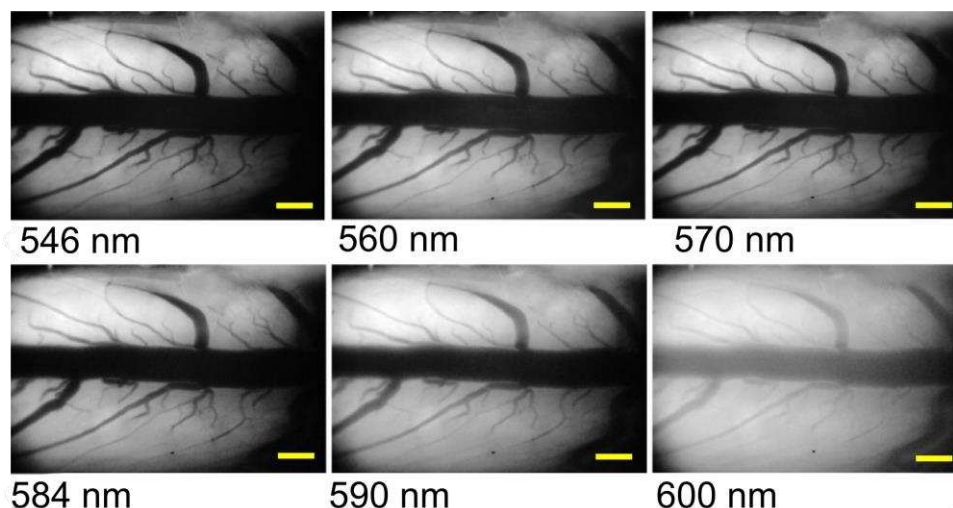
239 Multispectral images were successfully acquired at baseline normoxia 1, hyperoxia, normoxia 2, and
240 hypoxia 1 for all four rats. Rat 1 died before the hypoxia 2 oxygenation state (15% FiO_2), and thus
241 hypoxia 2 data are omitted for this rat. Representative multispectral images of rat spinal cord dorsal
242 vein are shown in Figure 5. The large dorsal vein lies on the dorsal surface of the spinal cord along the
243 rostral-caudal axis, with numerous smaller tributary veins. The large dorsal vein is too absorbing for
244 accurate oximetry, so tributary veins were analysed, provided they met the inclusion criteria described
245 in Section 2.2.

246

247 3.2. Response to changes in FiO_2

248 Average venous SO_2 values are shown in Figure 6. Corresponding arterial values, as measured by the
249 pulse oximeter, are also presented. As expected, average baseline venous SO_2 increased during
250 hyperoxia ($67.8 \pm 10.4\%$ [mean \pm standard deviation] increasing to $83.1 \pm 11.6\%$), and returned to
251 baseline values during the second state of normoxia ($67.4 \pm 10.9\%$) and further decreased during
252 subsequent hypoxic periods ($50.9 \pm 15.5\%$ and $29.2 \pm 24.6\%$ respectively). The differences in average
253 SO_2 between consecutive oxygenation states were all statistically significant ($p < 0.05$, pairwise t-test),
254 with changes between normoxia 1 and hyperoxia, hyperoxia and normoxia 2, and normoxia 2 and
255 hypoxia 1 all highly significant ($p < 0.01$). The normoxia baseline SO_2 values and changes due to FiO_2
256 interventions are physiologically plausible (normal venous SO_2 is typically $\sim 70\%$), helping to validate
257 our multispectral oximetry algorithm. The results for venous SO_2 for all individual animals are shown
258 in Figure 7 and Table 1. Vessel diameter measurements for all animals are summarised in Table 2,
259 including results of a pairwise t-test between all diameter values at consecutive oxygenation states –
260 which suggested no relationship between measured SO_2 and vessel calibre.

261



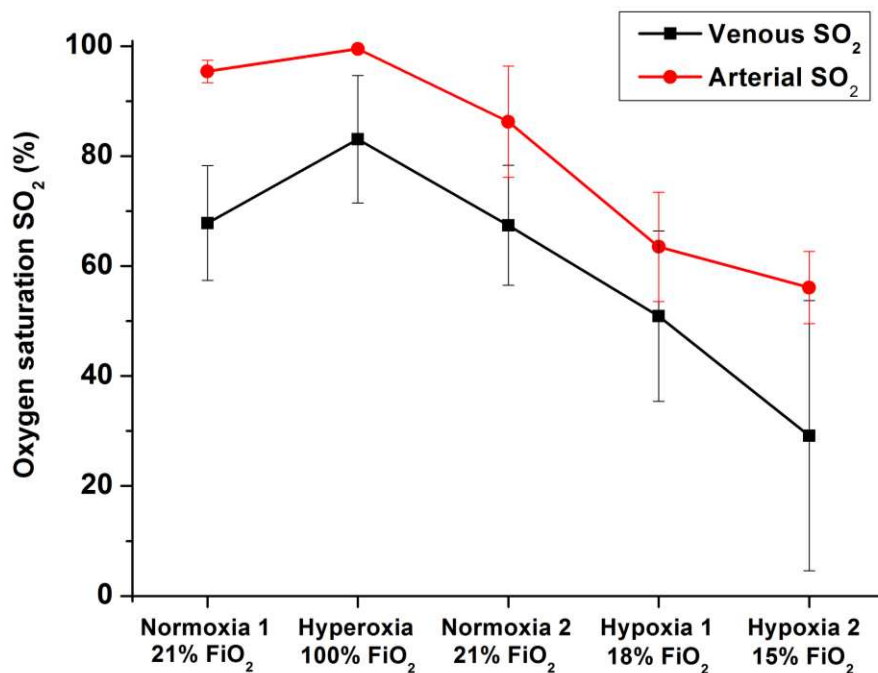
262
263 **Figure 5.** Multispectral images of spinal cord dorsal vein vasculature in a single rat. The main dorsal
264 vein lies on the dorsal surface of the spinal cord, with numerous tributary veins joining the larger vessel.
265 The scale bars represent 500 μm .

266 *3.3. Repeatability and inter-animal variability of measurements*

267 Repeatability of measurements was assessed by performing three measurements of SO_2 at baseline
268 normoxia for each individual rat, where physiological variations are expected to be minimal. The
269 average standard deviation of repeat measurements across all animals was $\pm 2.28\%$ SO_2 . This deviation
270 is much lower than changes in SO_2 observed due to variation of FiO_2 – which was above 15% between
271 normoxia and hyperoxia, and even greater for changes between normoxia and subsequent states of
272 hypoxia. This indicated sufficient repeatability over individual vessels for ascertaining changes in SO_2 .

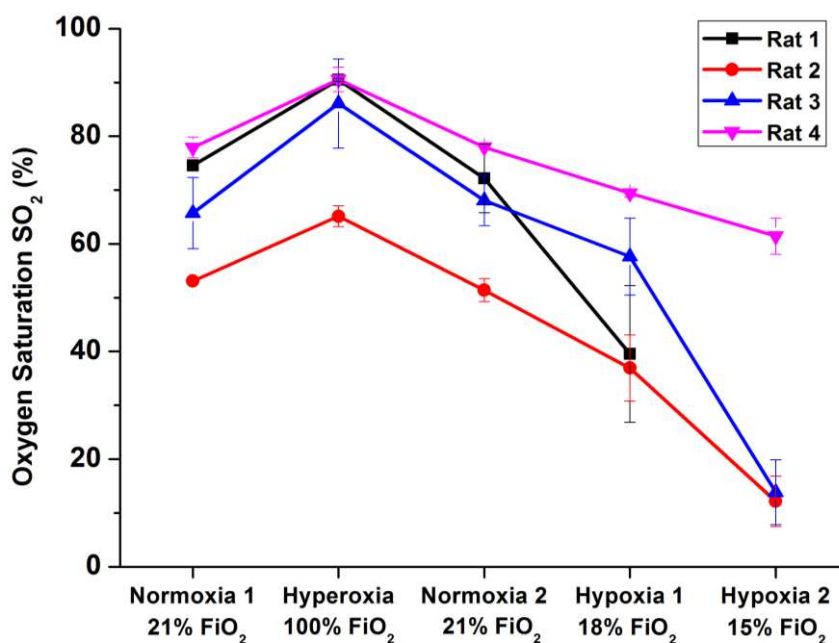
273 The changes in venous SO_2 observed throughout the experiment were strongly correlated with
274 changes in arterial SO_2 , as measured by the pulse oximeter. The calculated Pearson correlation
275 coefficients r were 0.74, 0.79, 0.87, and 0.88 for each rat respectively ($p < 0.01$). There was, however,
276 considerable variation in average baseline venous SO_2 between individual rats, ranging from 53% to
277 78% at normoxia. We did not find a correlation between this variation in venous SO_2 and the baseline
278 arterial SO_2 values. Some physiological variation is expected between rats due to potential differences
279 in depth of anaesthesia and the temperature of the exposed spinal cord (despite maintenance of rectal
280 temperature), both of which may affect venous oxygen saturation.

281



282
 283 **Figure 6.** Average venous SO₂ across all animals with variation in FiO₂. Corresponding average pulse
 284 oximeter data are also presented. Error bars represent the standard deviation of the average values of
 285 each individual rat.

286
 287
 288



289
 290 **Figure 7.** Variation in SO₂ with FiO₂ for each control rat. Results are the average value for each rat ±
 291 standard deviation.

292
 293

294

295 **Table 1.** SO₂ measurements for individual control rats.

	Average rat SO ₂ ± standard deviation (%)					Change (p-value)
	Rat 1	Rat 2	Rat 3	Rat 4	Average	
Normoxia 1 (21% FiO ₂)	74.6 ± 0.1	53.1 ± 0.5	65.8 ± 6.6	77.9 ± 1.9	67.8 ± 10.4	n/a
Hyperoxia (100% FiO ₂)	90.5 ± 0.3	65.2 ± 1.93	86.1 ± 8.3	90.6 ± 2.3	83.1 ± 11.6	<0.01
Normoxia 2 (21% FiO ₂)	72.2 ± 6.4	51.4 ± 2.1	68.1 ± 4.7	78.0 ± 0.2	67.4 ± 10.9	<0.01
Hypoxia 1 (18% FiO ₂)	39.6 ± 12.7	36.9 ± 6.2	57.7 ± 7.2	69.4 ± 0.7	50.9 ± 15.5	<0.01
Hypoxia 2 (15% FiO ₂)	N/A	12.2 ± 4.7	13.8 ± 6.00	61.5 ± 3.4	29.2 ± 24.6	<0.05

296

297 **Table 2.** Vessel diameter measurements throughout the experiment.

	Average vessel diameter ± standard deviation (µm)				Change (p-value)
	Rat 1	Rat 2	Rat 3	Rat 4	
Normoxia 1 (21% FiO ₂)	104.5 ± 0.9	87.7 ± 0.6	59.5 ± 1.4	100.5 ± 1.1	n/a
Hyperoxia (100% FiO ₂)	108.1 ± 0.6	89.8 ± 1.8	59.3 ± 1.4	103.0 ± 3.3	0.89
Normoxia 2 (21% FiO ₂)	105.5 ± 1.6	87.6 ± 0.7	57.9 ± 5.00	97.7 ± 1.3	0.81
Hypoxia 1 (18% FiO ₂)	107.0 ± 0.7	86.0 ± 0.7	60.8 ± 1.7	99.4 ± 1.4	0.88
Hypoxia 2 (15% FiO ₂)	N/A	81.7 ± 0.6	61.7 ± 1.3	99.3 ± 0.2	0.34

298

299

300 **4. Discussion**

301

302 *4.1. Performance of the multispectral microscope*

303 The multispectral microscope provided images of the dorsal vasculature of the rat spinal cord with
304 sufficient magnification and spectral contrast for oximetry of vessels approximately 50 to 130 µm in
305 diameter. Data acquisition was fully automated using a LabVIEW interface to minimise acquisition
306 time and potential human error. Further, the multispectral microscope was assembled with off-the-shelf
307 components, making it a relatively simple and cost-effective device. Using a digital SLR CMOS
308 detector was cost-efficient in comparison with scientific CCD or CMOS detectors, and provided
309 sufficient performance. Further reduction in cost could be achieved by replacing the LCTF with a bank
310 of bandpass filters. The LCTF has the advantage of rapid tuning and adaptability, but LCTF
311 transmission is low and it is the most costly component of the microscope. A computer-controlled filter

312 wheel would result in slower switching between wavebands, but this would be compensated by shorter
313 integration times afforded by higher optical throughput.

314 Integration time was less than 1 second for all wavelengths; for the 584 nm, 590 nm and 600
315 nm wavebands where LCTF transmission is higher, the integration time was as low as 100 ms.
316 Multispectral dataset acquisition rate was limited, however, by the LabVIEW SLR camera control
317 toolbox used (LabVIEW Camera Control for Nikon SLR, *Ackerman Automation*). The resulting data-
318 transfer speed was limited by the USB 2.0 capability of the SLR camera, which limited image
319 acquisition to once every 7.5 seconds. This resulted in an acquisition time of approximately 45 seconds
320 for a multispectral dataset. Acquisition time could be greatly improved in future by using a SLR camera
321 with USB 3.0 capability.

322

323 *4.2. Performance and validation of oximetry algorithm for in vivo imaging*

324 Our oximetry algorithm is based on an algorithm published by Smith et al. (2000) and we have used
325 empirical values of scattering coefficient, anisotropy factor, and extinction coefficients of oxygenated
326 and deoxygenated haemoglobin to provide a transmission-based model for estimation of SO₂. A
327 contrast-reduction parameter was also added to compensate for the effects of any tissue overlying blood
328 vessels.

329 Vessel diameter may influence other parameters in our algorithm, such as degree of optical scattering
330 and optical path length of light. In two-wavelength oximetry, for example, it has been reported that
331 large retinal veins are estimated to have a lower blood oxygen saturation than smaller veins (Hammer,
332 et al., 2008), but this may be a vein-diameter dependent calibration artefact in two-wavelength oximetry.
333 We found that fluctuations in diameter for a given vessel between consecutive oxygenation states were
334 not statistically significant (see Table 2).

335 It is clear from measurement that our oximetry analysis provides physiologically plausible
336 values for SO₂, is sensitive to changes in SO₂, and is insensitive to vessel diameter. However, highly
337 accurate validation of our oximetry algorithm remains challenging *in vivo*. Whilst the correlations with
338 arterial pulse oximeter data go some way towards explaining the variability in baseline venous SO₂,
339 verifying the absolute values produced by our technique is difficult. An option for an *in vitro* validation
340 study is to use whole *ex vivo* blood in transparent fluorinated ethylene propylene (FEP) capillaries,
341 placed on a diffuse white reflective background material such as Spectralon™. *In vitro* validation
342 requires variation of SO₂ in blood, generally achieved by addition of measured quantities of sodium
343 dithionite (Briely-Sabo & Bjornerud, 2000). However, sodium dithionite alters the osmolarity of blood
344 which affects optical properties, including scattering coefficients and anisotropy (Friebel, et al., 2010).
345 The development of a more realistic phantom and an alternative method to artificially deoxygenate
346 whole blood, such as the use of nitrogen gas, would be beneficial and will be considered for future
347 studies (Ghassemi, et al., 2015) (Denninghoff & Smith, 2000).

348 Many tributary vessels present in the images were too small (< 50 µm) to meet our inclusion
349 criteria: such vessels absorb light too weakly for accurate oximetry with the wavelengths used. To
350 enable analysis of smaller vessels, blue wavelengths (at which absorption is higher) could be
351 incorporated into the imaging scheme, providing sufficient contrast for accurate determination of
352 transmission profiles. This would increase the number of veins appropriate for analysis.

353

354 **5. Conclusions**

355

356 We have developed a cost-effective multispectral microscope to enable *in vivo*, calibration-free,
357 absolute oximetry of surgically-exposed dorsal veins of healthy rats. SO₂ and vessel diameters of
358 tributary dorsal veins were calculated for a range of inspired oxygen concentrations. This algorithm

359 yielded physiologically plausible values for SO₂ for each rat during normoxia, hyperoxia and graded
360 hypoxia, with SO₂ changing as expected. Further, these results correlated significantly with
361 corresponding arterial SO₂ values as determined by pulse oximetry.

362 The imaging system and oximetry technique provides sufficient sensitivity to SO₂ such that it
363 may be applied to the study of a variety of disease models where hypoxia may be a factor. The
364 preliminary results presented in this paper suggest that any significant changes in SO₂ related to specific
365 pathological changes will be quantifiable, and it is hoped that future studies using this technique will
366 provide a deeper understanding of disease pathology. The oximetry algorithm developed may be easily
367 extended to a wide range of other applications in future where localised SO₂ measurement is required
368 *in vivo*, such as oximetry in rodent models of multiple sclerosis, rheumatoid arthritis and non-invasive
369 retinal oximetry in humans.

370

371 **Acknowledgment**

372 This work was funded by the University of Glasgow Sensors Initiative and the Lord Kelvin Adam Smith
373 scholarship programme.

374

375 **References**

376

377 Beach, J. et al., 1999. Oximetry of retinal vessels by dual-wavelength imaging: calibration and
378 influence of pigmentation. *Journal of Applied Physiology*, pp. 748-758.

379 [Bosschaart, N. et al., 2014. A literature review and novel theoretical approach on the optical properties
380 of whole blood. *Lasers in Medical Science*, Volume 29, pp. 453-479.](#)

381 Briely-Sabo, K. & Bjornerud, A., 2000. Accurate de-oxygenation of ex vivo whole blood using
382 sodium Dithionite. *Proc. Intl. Sot. Mag. Reson. Med*, Volume 8, p. 2025.

383 [Cadotte, D. W. et al., 2012. Speckle variance optical coherence tomography of the rodent spinal cord:
384 in vivo feasibility. *Biomedical Optics Express*, 3\(5\), pp. 911-919.](#)

385 [Choudhary, T. R. et al., 2013. Assessment of acute mild hypoxia on retinal oxygen saturation using
386 snapshot retinal oximetry. *Investigative ophthalmology & visual science*, 54\(12\), pp. 7538-43.](#)

387 Davies, A. L. et al., 2013. Neurological Deficits Caused by Tissue Hypoxia in neuroinflammatory
388 disease. *Annals of Neurology*, 74(6), pp. 815-825.

389 [Denninghoff, K. & Smith, M., 2000. Optical model of the blood in large retinal vessels. *Journal of
390 Biomedical Optics*, 5\(4\), pp. 371-374.](#)

391 Desai, R. et al., 2016. Cause and prevention of demyelination in a model multiple sclerosis lesion.
392 *Annals of Neurology*, 79(4), pp. 591-604.

393 [Eltzschig, H. & Carmeliet, P., 2011. Hypoxia and Inflammation. *N Engl J Med*, Volume 364, pp. 656-
394 65.](#)

395 [Faber, D. J. et al., 2004. Oxygen Saturation-Dependent Absorption and Scattering of Blood. *Physics
396 Review Letters*, 93\(2\).](#)

397 Figley, S. A. et al., 2013. A Spinal Cord Window Chamber Model for In Vivo Longitudinal
398 Multimodal Optical and Acoustic Imaging in a Murine Model. *PLOS one*, 8(3).

- 399 Friebel, M., Helfmann, J. & Meinke, M. C., 2010. Influence of osmolarity on the optical properties of
400 human erythrocytes. *J. Biomed. Opt.*, 15(5).
- 401 Ghassemi, P. et al., 2015. Rapid prototyping of biomimetic vascular phantoms for hyperspectral
402 reflectance imaging. *Journal of Biomedical Optics*, 20(12).
- 403 Hammer, M., Vilser, W., Riemer, T. & Schweitzer, D., 2008. Retinal vessel oximetry-calibration,
404 compensation for vessel diameter and fundus pigmentation, and reproducibility. *J. Biomed Opt.*,
405 13(5).
- 406 Johannssen, H. C. & Helmchen, F., 2010. In vivo Ca²⁺ imaging of dorsal horn neuronal populations
407 in mouse spinal cord. *The Journal of physiology*, 588(18), pp. 3397-3402.
- 408 Lesage, F., Brieb, N., Dubeaub, S. & Beaumont, E., 2009. Optical imaging of vascular and metabolic
409 responses in the lumbar spinal cord after T10 transection in rats. *Neuroscience letters*, 454(1), pp.
410 105-109.
- 411 MacKenzie, L., Choudhary, T., McNaught, A. & Harvey, A., 2016. In vivo oximetry of human bulbar
412 conjunctival and episcleral microvasculature using snapshot multispectral imaging. *Experimental Eye*
413 *Research*.
- 414 Mordant, D. et al., 2011. Spectral imaging of the retina. *Eye*, Volume 25, pp. 309-320.
- 415 Prah, S., 1999. Optical Absorption of Hemoglobin. *Oregon Medical Laser Center*,
416 <http://omlc.org/spectra/hemoglobin/index.html>.
- 417 Schweitzer, D. et al., 1995. Calibration-free measurement of the oxygen saturation in retinal vessels
418 of men. *Proc. SPIE, Ophthalmic Technologies V*, 2393(210).
- 419 Sharma, V. et al., 2011. Quantification of light reflectance spectroscopy and its application:
420 Determination of hemodynamics on the rat spinal cord and brain induced by electrical stimulation.
421 *NeuroImage*, 56(3), pp. 1316-1328.
- 422 Smith, M., 1999. Optimum wavelength combinations for retinal vessel oximetry. *Applied optics*,
423 38(1), pp. 258-67.
- 424 Smith, M. H., Denninghoff, K. R., Lompad, A. & Hillman, a. L. W., 2000. Effect of multiple light
425 paths on retinal vessel oximetry. *Applied Optics*, 39(7), pp. 1183-93.
- 426 Sorg, B. S. et al., 2005. Hyperspectral imaging of hemoglobin saturation in tumor microvasculature
427 and tumor hypoxia development. *Journal of biomedical optics*, 10(4).
- 428 Taylor, P. C. & Sivakumar, B., 2005. Hypoxia and angiogenesis in rheumatoid arthritis. *Current*
429 *opinion in rheumatology*, Volume 17, pp. 293-298.
- 430 Vinegoni, C., Lee, S., Feruglio, P. F. & Weissleder, R., 2014. Advanced Motion Compensation
431 Methods for Intravital Optical Microscopy. *IEEE Journal of Selected Topics in Quantum Electronics*,
432 20(2).
- 433 Zijlstra, W., Buursmaa, A., Falke, H. & Catsburg, J., 1994. Spectrophotometry of hemoglobin:
434 absorption spectra of rat oxyhemoglobin, deoxyhemoglobin, carboxyhemoglobin, and
435 methemoglobin. *Comp. Biochem. Physiol.*, 107B(1), pp. 161-166.
- 436